mater.scichina.com link.springer.com

Sci China Mater 2026, 69(2): 838–847
https://doi.org/10.1007/s40843-025-3712-2

Controlling ligand field of Li_3VO_4 to enhance the electrochemical performance for lithium-ion batteries

Jidong Ma[1,2†], Heng Liu[3†], Te Kang[3], Changyuan Li[3], Huanhuan Niu[3], Long Yang[3], Chaofeng Liu[2,3*] and Guozhong Cao[2*]

ABSTRACT Electrochemical potential and ion diffusion of electrode materials restrain the energy and power densities of lithium-ion batteries, and these challenges also remain in the intercalation-type Li_3VO_4 (LVO). In this work, the local [VO_4] coordination symmetry in LVO is broken by a higher concentration of oxygen vacancies (Vö), resulting in an increased average V–O bond length and a larger ligand field splitting. These alterations reduce the energy level of the lowest unoccupied orbitals (e^*) and lift the electrochemical potential, resulting in a higher voltage output. Additionally, the broken local symmetry in Vö-LVO is found to reduce the band gap and expand the ion transport channels, which favors enhancing electronic conductivity and facilitates ion diffusion, thereby improving the electrochemical kinetics in the energy storage process. The local symmetry broken sample (Vö-LVO) achieves a significantly improved capacity of 532 mAh/g at 0.1 A/g in comparison with 394 mAh/g of pristine LVO, and long cycling stability with retained capacity of 398 mAh/g at 1 A/g over 500 cycles compared with 236 mAh/g of the pristine LVO. The fundamental understanding paves the way to exploit high-performance electrodes via ligand field engineering for next-generation rechargeable batteries.

Keywords: Li_3VO_4, ligand field, working voltage, ion diffusion, lithium-ion batteries

INTRODUCTION

Lithium-ion batteries (LIBs) are widely used in portable electronics, electric vehicles, and large-scale energy storage systems [1–3]. As an essential component of LIBs, anode materials play an important role in determining the comprehensive performance of the batteries [4–6]. Graphite is dominantly used as the anode material in commercial LIBs, but it is limited by its low theoretical capacity (372 mAh/g) and safety issues (Li dendrite, a potential cause of short circuit) [7–10]. $Li_4Ti_5O_{12}$, another important member in the anode family, has high lithium ion diffusion coefficient (10^{-9}–10^{-13} cm^2/s), excellent rate capability, and safety with electrolytes [11]. However, its low theoretical capacity (175 mAh/g) and relatively high lithium insertion/extraction voltage (~1.55 V vs. Li^+/Li) limit the voltage output and energy density of full batteries [12–14]. Li_3VO_4 (LVO), as an emerging anode material based on intercalation reactions, has a lower lithium ion intercalation voltage region (0.5–1.0 V vs. Li^+/Li) and a higher specific capacity (592 mAh/g with 3 Li^+ inserted) [15,16]. The discharge voltage of LVO is slightly higher than that of graphite, and effectively avoids the growth of lithium dendrites and serious electrolyte decomposition. However, its relatively low electronic conductivity ($<10^{-10}$ S/cm) results in poor rate performance and large polarization, preventing its large-scale commercial application [17–19]. To address these challenges and enhance the electrochemical performance of LVO, various strategies such as nanostructure design [15,20,21], coating [17,22–25], compositing [26–30], and doping [16,31–33], have been widely explored. Nanostructured LVO particles synthesized by the hydrothermal method with an average size of 250 nm present larger surface area, shorter lithium diffusion paths, and better strain accommodation, leading to enhanced lithium storage capacity, improved rate capability and cycling stability [21]. Coating is to deposit a thin guest layer on the surface of LVO particles to improve electrical conductivity, enhance surface stability or modify the morphology of LVO [34,35]. Coatings are mostly made from carbonaceous materials (e.g., graphitized carbon, amorphous carbon) [25,36]. The coating of highly graphitized carbon material with micrometer sizes provides a conductive network and porous ion transport channels, ensuring rapid mass transfer [36]. This coating also modifies the morphology of Li_3VO_4, forming Li_3VO_4 nanoparticles with an average diameter of ~30 nm to offer a high electrochemical activity [36]. The amorphous carbon coating provides a protective layer against side reactions with electrolytes and structure collapse during cycling processes, thereby improving the overall electrochemical performance of the LVO electrode [25]. Compositing LVO with carbon materials (e.g., reduced graphene oxide, carbon nanotube, graphene) [26,37,38], $Ti_3C_2T_x$ MXene [30], and NiO/Ni [39], to form a hierarchical structure, is another strategy to enhance the electrochemical activity of LVO. For instance, by homogeneously anchoring LVO nanoparticles on carbon nanofibers, the formed Li_3VO_4@C nanofibers with a diameter of 200–400 nm show high reactivity, enhanced electronic conductivity, and reduced volume changes during cycling [40]. Doping is also an effective and efficient approach; the guest atoms have different valence states or ionic radii compared to vanadium and lithium, bene-

---

[1] Fujian Provincial Key Laboratory of Functional Materials and Applications, Xiamen University of Technology, Xiamen 361024, China
[2] Department of Materials Science and Engineering, University of Washington, Seattle, WA 98195, USA
[3] School of Materials Science and Engineering, Tongji University, Shanghai 201804, China

[†] Equally contributed to this work.

[*] Corresponding author (email: chaofeng@tongji.edu.cn; gzcao@uwashington.edu)

ficial to modify their intrinsic properties [32,33,41,42]. Mo^{6+} replaced partial V^{5+} in LVO introduces extra electrons, increasing the concentration of electronic charge carriers and forming n-type semiconductor, which significantly improves the electronic conductivity [32]. The doping of Li^+ sites in LVO by Mg^{2+} ions can also improve the electronic conductivity, stabilize the crystal structure, and enhance the lithium diffusion kinetics of LVO [33]. Introducing ionic defects, such as oxygen vacancies, through heating treatment is also an effective and facile strategy to improve the electronic conductivity, transfer kinetics, structural stability and increase the amount of active storage sites [43,44]. In particular, oxygen vacancies (Vö) are widely investigated due to their low formation energy, which tend to form under low oxygen pressure or reduction atmosphere. Introducing oxygen vacancies has been demonstrated to improve electronic conductivity, transfer kinetics, structural stability and increase the amount of active storage sites [45]. Although the electrochemical performance of LVO has enhanced considerably owing to these modifications, progress in modulating its working voltage still remains sluggish. This research gap underscores in-depth investigations into regulating the chemical coordination structure of LVO, which enhances the transfer kinetics and dominates the ligand field of electrode materials, determining the working voltage [46].

In this work, the local $[VO_4]$ coordination symmetry of LVO is broken through annealing in nitrogen. The obtained sample is named Vö-LVO. Multiple characterizations have demonstrated that the higher concentration of oxygen vacancies induced by annealing in Vö-LVO breaks the local symmetry and increases the average V–O bond length of Vö-LVO. The elongated average V–O distance reduces the repulsion between the electrons of V 3d and O 2p, altering the crystal field and lowering the energy of V 3d orbitals. The broken local symmetry of $[VO_4]$ tetrahedra in Vö-LVO leads to a secondary splitting of V 3d orbitals and further splitting the ligand field. These change in electronic structure reduces the energy level of the lowest unoccupied orbitals (e^*); thereby Vö-LVO achieves a higher working voltage compared with LVO. Additionally, compared with LVO, local symmetry broken Vö-LVO shows improved electronic conductivity, faster ion diffusion, realizing fast and reversible Li^+ storage and much improved battery performances.

RESULTS AND DISCUSSION

The facile and low-cost synthesis process is schematically illustrated in Fig. S1. First, all raw materials were dissolved into water to form transparent solutions. Then the water was evaporated assisted with heat and the solutions turned to powders. Finally, Vö-LVO and LVO were annealed at 600 °C for 2 h in nitrogen and air, respectively. For Vö-LVO, the elevated temperature facilitates the diffusion of oxygen atoms to the surface to react with nitrogen gas. In addition, the nitrogen atmosphere, where the partial oxygen pressure is too low, lacks available oxygen sources to replenish the oxygen atoms. Fig. S2 shows the thermogravimetry (TG) curves of both samples, which were conducted in air, heating at 10 °C/min from room temperature (RT) to 700 °C. The oxygen vacancies within the lattice lead to the absorption of oxygen when heated in air, resulting in the mass increase. In Fig. S2, Vö-LVO shows mass increase of 0.45%, higher than that of LVO, further validating the higher concentration of oxygen vacancies in Vö-LVO. Consequently, oxygen vacancies are formed to break the local coordination symmetry in the crystal structure. Fig. 1a shows X-ray diffraction (XRD) patterns of both samples and the Rietveld refinement method is used to analyze the detailed crystal structure information of Vö-LVO (Fig. 1b) and LVO (Fig. S3). Detailed structural information, including the lattice parameters, atomic positions of both samples, is summarized in Table S1. The diffraction peaks of both samples are indexed well with the orthorhombic phase of LVO (JCPDS NO.38-1247) with a space group *Pnm*21, indicating that Vö-LVO retains the same crystal structure as LVO. The crystal structure of LVO is constructed with the corner-sharing $[LiO_4]$ and $[VO_4]$ tetrahedra. Scanning electron microscopy (SEM) images of Vö-LVO and LVO are shown in Fig. S4a, b. Both samples have irregular agglomerated particles, revealing that annealing in nitrogen or air makes no appreciable impact on microstructure. High-resolution transmission electron microscopy (HRTEM) images in Fig. S4c, d reveal the lattice spacing of 0.389 nm corresponds to the *d*-spacing of (011) facets of Li_3VO_4, indicating the introduction of oxygen vacancies has no detectable impacts on the lattice constants, which is corroborated well with the results of XRD refinement. However, Vö-LVO and LVO samples show an obvious color difference. The Vö-LVO sample is gray, while the LVO sample is white (Fig. S1). The color difference relates to defects and electronic structure in the samples. Fig. 1c shows the O 1s X-ray photoelectron spectroscopy (XPS) of both samples and the XPS survey spectra are shown in Fig. S5. The characteristic peaks at about 530.0 eV correspond to the lattice oxygen. The peaks at ~531.7 eV are attributed to oxygen vacancies and the peaks at about 533.1 eV originate from adsorbed water species [47–49]. The area of the Vö peak in Vö-LVO accounts for 13% of the total peak, which is higher than the 8% in LVO, indicating the higher concentration of oxygen vacancies in Vö-LVO, which results from the low partial oxygen pressure atmosphere (N_2) facilitating the formation of oxygen vacancies. Fig. S6 shows the Raman spectra of both samples. The peaks within the range of 300–400 cm^{-1} are attributed to the bending vibration mode of V–O bonds in $[VO_4]$ tetrahedra [50]. The loss of lattice oxygen in Vö-LVO breaks the corresponding V–O bonds, turning the doublet bending vibration peaks of LVO into the singlet of Vö-LVO. The higher concentration of oxygen vacancies in Vö-LVO also results in its lower intensity of Li–O stretching vibration at 451 cm^{-1} [51], compared with that of LVO, due to the partial breaking of Li–O bonds. The peaks range from 700 to 950 cm^{-1} originate from the stretching vibration mode of V–O bonds in $[VO_4]$ tetrahedra [50,52]. Fig. S7 shows the Fourier transform infrared (FTIR) spectra of both samples. The peak at ~712 cm^{-1} is attributed to the asymmetric stretching vibration of V–O bonds [16,53]. The wavenumber of the O–H bond peak in Vö-LVO experiences a blue shift, indicating an increase in the strength of the O–H bond. This is likely due to the presence of more oxygen vacancies on the Vö-LVO surface, allowing for water molecules to be more prone to adsorption on the crystal surface or near the vacancies, leading to stronger binding between the water molecules and the surface. Fig. 1d shows the V K-edge X-ray absorption spectroscopy (XAS) of both samples. The pre-edge peak at ~5469.5 eV reflects the transitions from V 1s to p-hybridized V 3d states and the peak intensity relates to the coordination geometry [54]. A higher intensity indicates a lower central symmetry in the coordination polyhedral [55–57]. Vö-LVO lost its partial coordination oxygen in $[VO_4]$ polyhedron

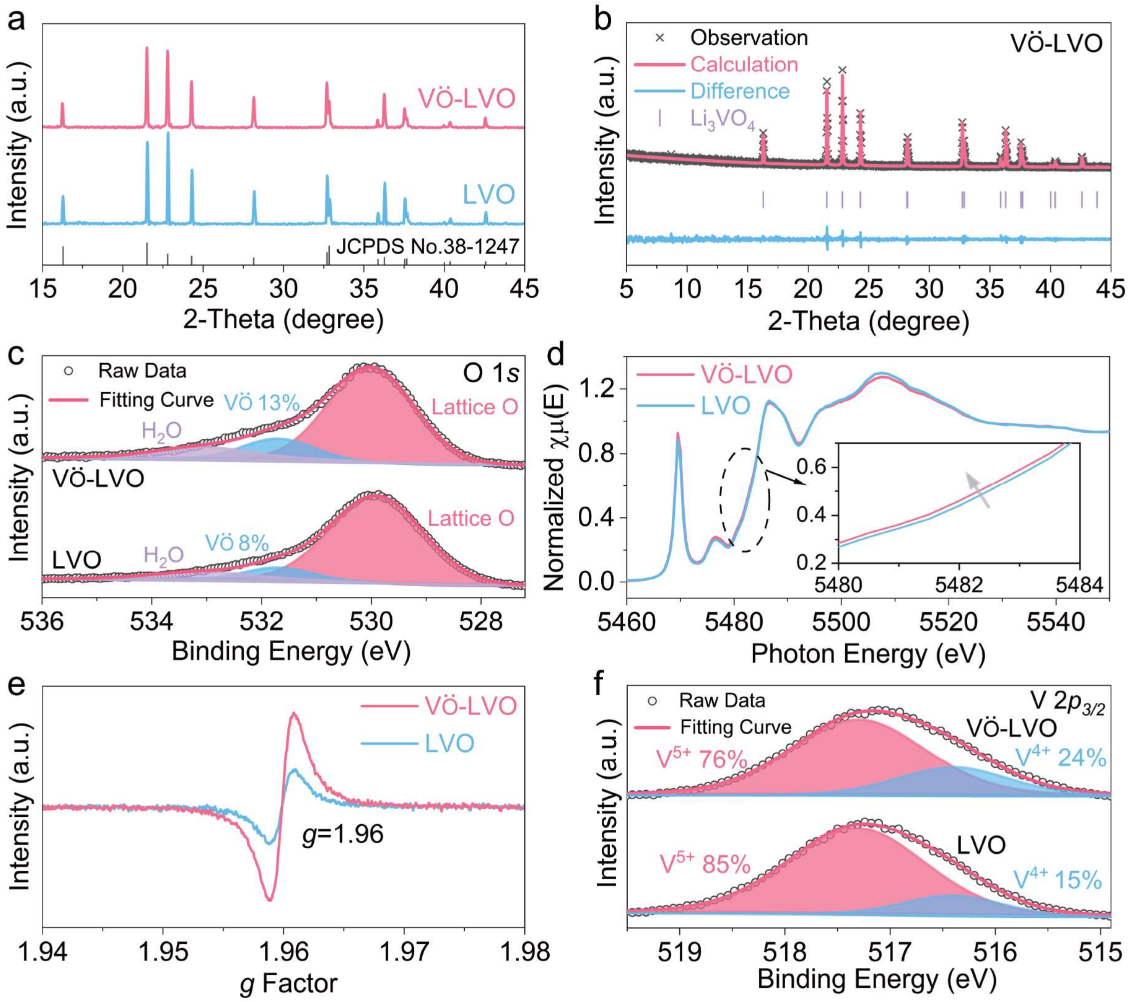

Figure 1 (a) XRD patterns of the Vö-LVO and LVO samples. (b) XRD pattern of Vö-LVO with Rietveld refinement. (c) XPS spectra of O 1s for Vö-LVO and LVO. (d) XAFS spectra of the V K-edge for Vö-LVO and LVO. (e) EPR spectra of Vö-LVO and LVO. (f) XPS spectra of V $2p_{3/2}$ for Vö-LVO and LVO.

causing the broken symmetry, reflecting in the higher pre-edge peak intensity of Vö-LVO. The absorption edge position of the V K-edge X-ray absorption near-edge structure (XANES) corresponds to the chemical states of vanadium in both samples. Compared with LVO, the shift of Vö-LVO toward lower energy suggests that partial V^{5+} is transformed to V^{4+}. As previously discussed, Vö-LVO has a higher concentration of oxygen vacancies, which tends to reduce V^{5+} to a lower valence state due to the electroneutrality requirement in the lattice. V^{4+} in both the surface and the bulk can also be detected by the electron paramagnetic resonance (EPR) spectra. As shown in Fig. 1e, signals with a g value of 1.96 were detected in both Vö-LVO and LVO, corresponding to the unpaired $3d^1$ electrons in V^{4+} [58]. While V^{5+} is EPR silent because of its $[Ar]3d^0$ electron structure containing no unpaired electron. Vö-LVO shows stronger signal intensity than LVO, indicating an increased amount of V^{4+} species in Vö-LVO, consistent with the XANES spectra discussed above. Fig. 1f shows the fitting results of V $2p_{3/2}$ XPS of both samples. Charging calibration has been performed based on the C 1s peak at 284.8 eV corresponding to adventitious carbon. The value of $V^{4+}/(V^{4+}+V^{5+})$ in Vö-LVO is 24%, higher than that of LVO (15%), further verifying the larger proportion of V^{4+} in Vö-LVO. Tetravalent and pentavalent vanadium ions have different electronic structures and thus cause different absorption wavelengths [59].

Fig. 2a is the chemical bond information derived from V K-edge extended X-ray absorption fine structure (EXAFS) in R space to demonstrate the changes in the local coordination structure induced by oxygen vacancies. The strongest peak is attributed to the V–O bond length. Vö-LVO shows a longer V–O bond length of 1.65 Å than 1.62 Å of LVO, suggesting the larger average V–O bond length in Vö-LVO. Compared with LVO, Vö-LVO has a higher ratio of V^{4+}, which has a larger ionic radius than V^{5+}, leading to the longer V–O bonds in Vö-LVO [60]. The decreased V–O peak intensity in Vö-LVO indicates its lower V–O coordination number than LVO [56], which further validates the higher concentration of oxygen vacancies in Vö-LVO. The peak at ~2.89 Å relates to the V–O distance of the second coordination shell [56], and the diminished peak intensity further validates the lower V–O coordination number in Vö-LVO. Specifically, the longer bond length in average and the lower V–O coordination number in Vö-LVO indicate its higher degree of structural disorder and reduced symmetry. Furthermore, Fig. 2b, c show the fitting curves of R space and its imaginary part, which were performed from 0 to 3 Å, mainly contributed by the first V–O coordination shell (Tables S2 and

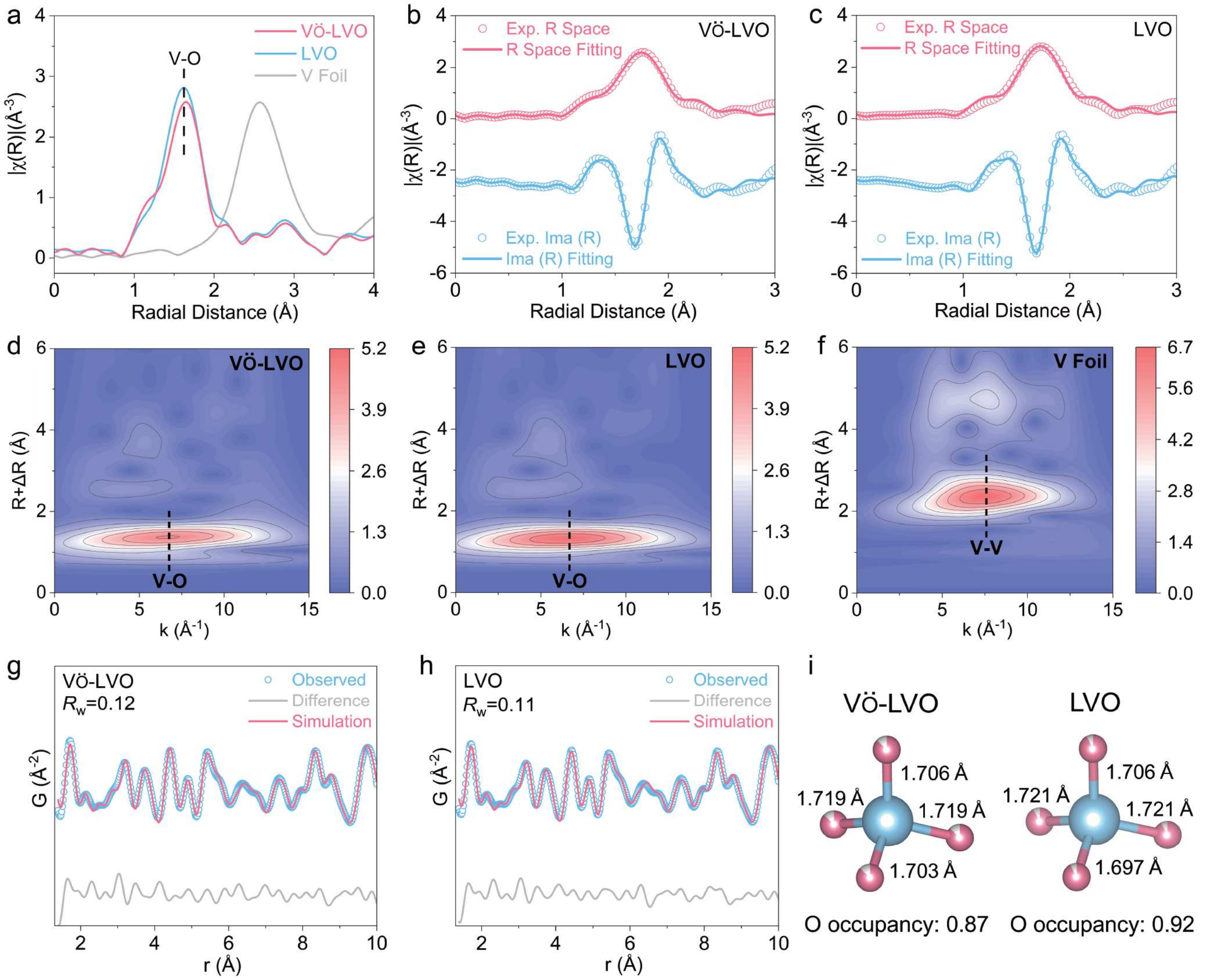

Figure 2 (a) k^2-weighted Fourier transform of the V K-edge EXAFS. V K-edge EXAFS data points and the fitting curves of (b) Vö-LVO and (c) LVO. WT of EXAFS for (d) Vö-LVO, (e) LVO and (f) V foil. X-ray PDF refinement results of (g) Vö-LVO and (h) LVO. (i) Schematic illustration of the tetrahedral distortion in Vö-LVO and LVO resolved by PDF refinements.

S3). The coordination numbers of Vö-LVO and LVO are approximately 3.38 and 3.95, respectively. The reduced coordination number suggests the higher concentration of oxygen vacancies in the Vö-LVO sample. The V–O distance of the first V–O coordination shell in Vö-LVO and LVO are 1.717 and 1.708 Å, respectively, further indicating the elongated V–O bond length on average. The wavelet transform (WT) of EXAFS for Vö-LVO, LVO and V foil (Fig. 2d–f) confirms that the V–O scattering has a shell domain with a local maximum at R = 1.38 Å and k = 6.61 Å^{-1} in Vö-LVO, and a slight shift R = 1.34 Å and k = 6.35 Å^{-1} in LVO; both of them differ from the V–V scattering at R = 2.5 Å and k = 7 Å^{-1} of V foil in Fig. 2f. The R in the wavelet transform is shorter than that in Fig. 2a because of the phase shift. Fig. 2g, h are the synchrotron X-ray pair distribution function (PDF) data and the refinement results of both samples. Fig. S8 shows the partial PDF curves of both samples, which illustrate the contribution of each atomic pair to the total PDF peaks. For both samples, the PDF peak at ~1.7 Å corresponds to the V–O bond length in [VO$_4$] tetrahedra and the peak at ~2.1 Å is contributed by the Li–O interatomic distance within the first coordination shell. The peak at about 3.1 Å is attributed to Li–V and O–O distances. The peak at ~3.7 Å is mostly contributed by the V–O pair distances of the second coordination shell. The peaks that have a larger radial distance than 4 Å originate from the integration of V–O, O–O, V–V, Li–O, Li–Li and Li–V interatomic distances beyond the first coordination shell. Vö-LVO shows a similar PDF pattern with LVO but lower oxygen occupancy (0.86) than that of LVO (0.92), indicating the higher concentration of oxygen vacancies in Vö-LVO. Fig. 2i shows the [VO$_4$] tetrahedron of both samples obtained from PDF local structural refinements. The refined lattice parameters are shown in Table S4. For the four V–O bonds in the [VO$_4$] tetrahedron, two bonds are shortened from 1.721 Å in LVO to 1.719 Å in Vö-LVO, by 0.002 Å. Meanwhile, one V–O bond is elongated from 1.697 Å in LVO to 1.703 Å in Vö-LVO, by 0.006 Å. The remaining one in both samples shows identical length. On average, the V–O bond length in Vö-LVO is longer than that of LVO, consistent with the results of EXAFS. According to the ligand field theory, the larger average V–O bond length reduces the electrostatic repulsion between the electrons of vanadium and oxygen, bringing V 3d orbitals (e and t$_2$ in four-fold coordination) to lower energy level [46]. In addition, the introduction of oxygen vacancies breaks the local symmetry and also decreases the repulsion between the electrons of O and V, further reducing V 3d to a lower energy, which strongly relates to the voltage [61]. To figure out the specific effects of the local structure changes in [VO_4] tetrahedron on the orbital energy and the working voltage of Vö-LVO, multi-scale electronic structure calculations and characterizations are performed.

Fig. 3a, b show the total density of states (TDOS) for Vö-LVO and theoretically perfect LVO without oxygen vacancies, respectively. The valence band (VB) is mainly composed of O 2p [19,62]. V 3d, which splits into e ($3d_{z^2}$ and $3d_{x^2-y^2}$) and t_2 ($3d_{xy}$, $3d_{yz}$ and $3d_{xz}$) orbitals in [VO_4] tetrahedra [63], contributes highly to the conduction band (CB). Specifically, the e and t_2 orbitals develop an anti-bonding interaction with O 2p orbitals, forming e^* (O 2p–$3d_{z^2}$ or $3d_{x^2-y^2}$) and t_2^* (O 2p–$3d_{xy}$, $3d_{yz}$ or $3d_{xz}$) anti-bonding orbitals, which constitute the CB [46]. For Vö-LVO and LVO, which are dominated by V^{5+}, e^* anti-bonding orbitals are the lowest unoccupied state and determine the voltage of the electrode. With a higher concentration of oxygen vacancies, the local symmetry of [VO_4] tetrahedra is broken and the asymmetric crystal field results in the more significant splitting of e^* and t_2^* states in Vö-LVO. In addition, both the CB and VB in Vö-LVO show a significant shift to lower energy due to this altered ligand field. The splitting of e^* and the shift of VB/CB contribute to the decreased band gap, as shown in Fig. 3c. The band gap (E_g) can be evaluated through the plot $(\alpha h\nu)^2$ versus photon energy $h\nu$. In the function, α is the absorption coefficient, $h\nu$ is the photon energy. By extrapolating to $(\alpha h\nu)^2 = 0$, the estimated band gaps are 3.18 and 3.28 eV for Vö-LVO and LVO, respectively. The narrower band gap of Vö-LVO contributes to its better electronic conductivity. The V L-edge and O K-edge XANES spectra are shown in Fig. S9. The higher peak intensities of O K-edge demonstrate the higher covalency of V–O bonds due to the shortened bond length [64]. Fig. 3d shows the peaks of e^* and t_2^* anti-bonding states in O K-edge XANES spectra for both samples. The e^* peak of Vö-LVO shows a left shift compared with LVO, further verifying the lower energy

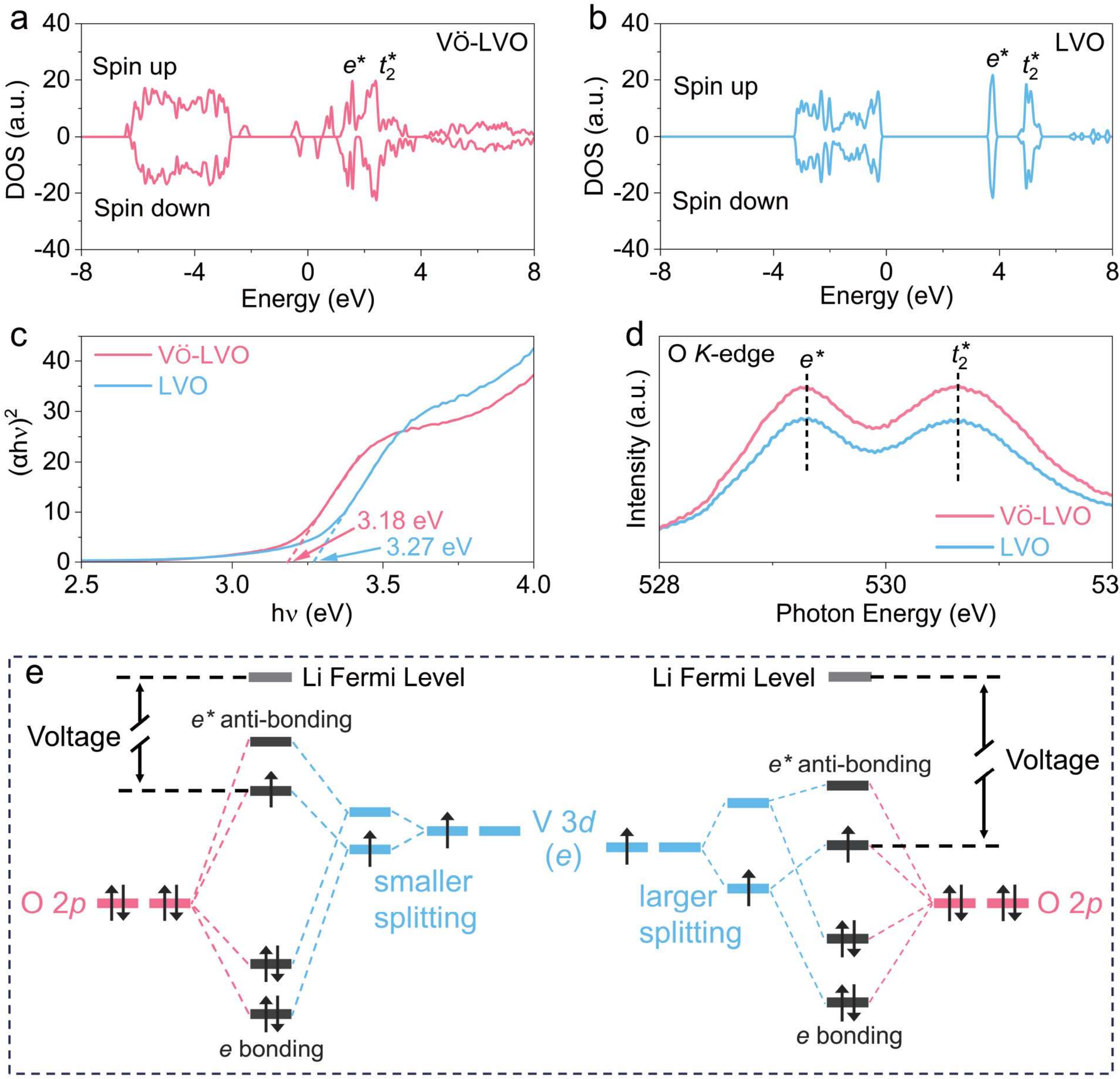

Figure 3 Calculated TDOS of (a) Vö-LVO and (b) LVO. (c) Plots of $(\alpha h\nu)^2$ and $h\nu$ obtained from the ultraviolet-visible absorption spectra of both samples. (d) O K-edge XANES spectra of both samples. (e) Schematic illustration of orbital hybridization in Vö-LVO and LVO.

level of e^* state, which is the lowest unoccupied state in V^{5+} and determines the electrochemical potential. Fig. 3e is the schematic illustration of the ligand field of Vö-LVO and LVO. In a tetrahedral crystal field, the e orbitals of V 3d consist of two-fold degenerate orbitals: $3d_{z^2}$ or $3d_{x^2-y^2}$. The introduction of oxygen vacancies in Vö-LVO breaks the local symmetry of $[VO_4]$ tetrahedra, leading to the splitting of the degenerate e orbitals into two non-degenerate orbitals with different energy levels. The split e orbitals further form bonding/anti-bonding molecular orbitals with O 2p orbitals, subsequently resulting in the splitting of e bonding and e^* anti-bonding orbitals. In this case, e bonding orbitals and e^* anti-bonding orbitals in Vö-LVO all decrease to lower energy compared with LVO, which has been demonstrated by the TDOS and O K-edge XANES spectra in Fig. 3a, b and d. This decreased orbital energy in Vö-LVO is due to its higher concentration of oxygen vacancies, resulting in more significant splitting than that in LVO. Moreover, the longer average V–O bond length in Vö-LVO reduces the repulsion exerted on V 3d electrons by O 2p electrons, reducing the V 3d energy and ulteriorly decreasing the energy of e bonding and e^* anti-bonding orbitals. The electronic configurations of V^{5+} and V^{4+} are [Ar] and $[Ar]3d^1$, respectively. For Vö-LVO and LVO, the single 3d electron of V^{4+} occupies a portion of e^* anti-bonding orbitals, which determines the voltage of the electrode. Therefore, Vö-LVO with lower e^* energy enlarges its energy gap between the Fermi level of zinc metal and has a higher voltage.

The electrochemical properties and battery performances of Vö-LVO and LVO as anode materials are evaluated in a half-cell configuration. Fig. S10 shows the N_2 adsorption-desorption isotherm along with the corresponding pore size distribution and Brunauer-Emmett-Teller (BET) surface area for Vö-LVO and LVO. Note that the BET method shows insufficient accuracy for micropores (<2 nm) and mainly focuses on the mesopores beyond 2 nm. Fig. S4a, b indicate a similar pore size distribution and adsorption behavior in both samples. The BET results demonstrate Vö-LVO and LVO have a similar pore size distribution and specific surface area, and the difference in the electrochemical performance is mainly attributed to the lattice modification rather than the microstructures as discussed above. The rate capabilities of the Vö-LVO and LVO electrodes are compared in Fig. 4a. At the current densities of 0.1, 0.2, 0.5, 1, 2, 4 and 8 A/g, the specific capacities of the Vö-LVO electrode are 532, 482, 397, 325, 255, 190 and 137 mAh/g. The specific capacity at 8 A/g remains 26% of that at 0.1 A/g. Upon reverting to a current density of 0.1 A/g, Vö-LVO demonstrates a specific capacity restoration to 528 mAh/g, highlighting its excellent reversibility. The specific capacities of the Vö-LVO electrode are much higher than those of the LVO electrode at all current densities (394, 336, 259, 206, 159, 122 and 94 mAh/g at the current densities of 0.1, 0.2, 0.5, 1, 2, 4 and 8 A/g, respectively).

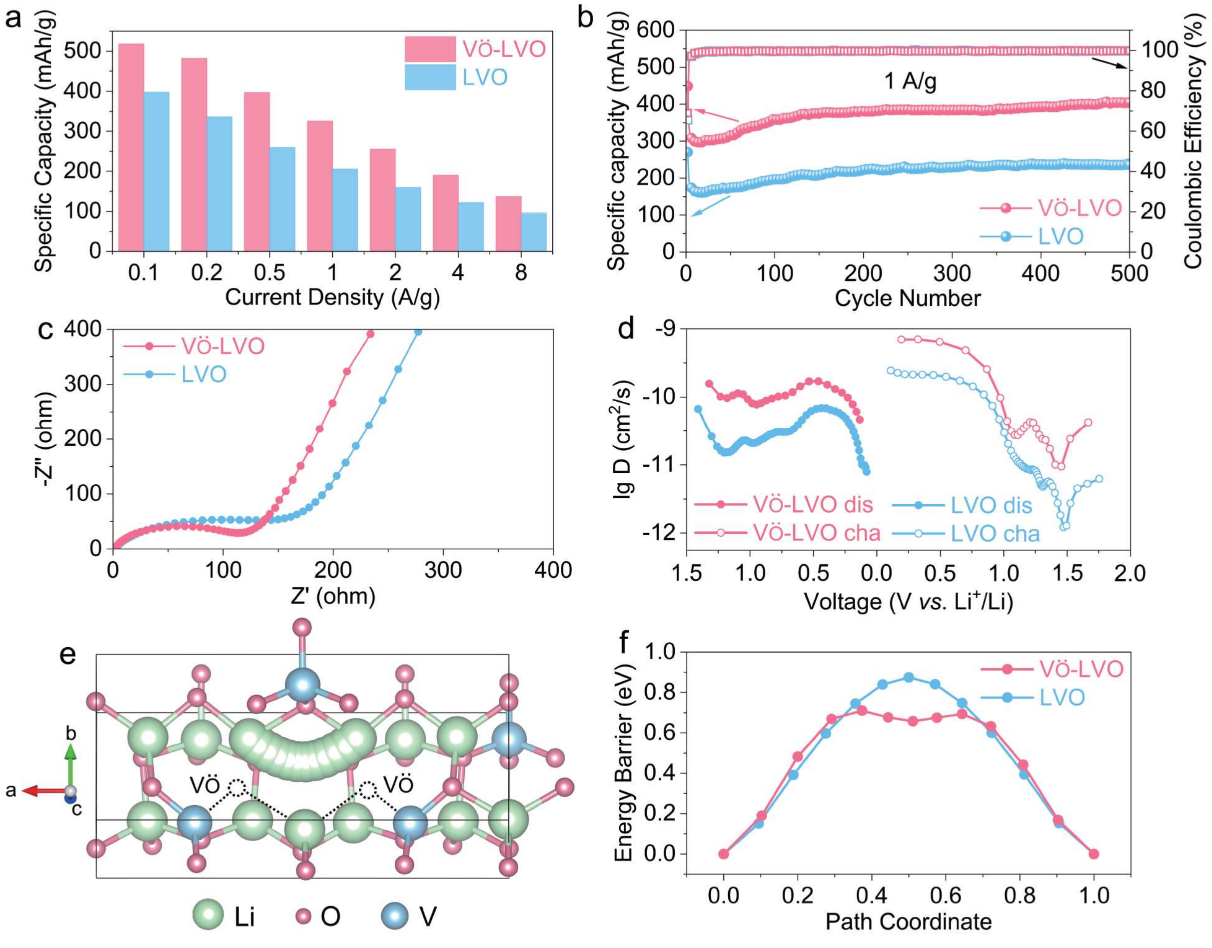

Figure 4 (a) Rate capability of Vö-LVO and LVO in the voltage range of 0.01–3.00 V versus Li/Li^+. (b) Cycling stability of Vö-LVO and LVO at a current density of 1 A/g for 500 cycles. (c) Nyquist plots of Vö-LVO and LVO electrodes before cycling tests. (d) Li^+ diffusion coefficients from GITT tests. (e) Li^+ diffusion pathways along the *a*-axis in Vö-LVO and LVO. (f) Calculated Li^+ diffusion energy barriers in Vö-LVO and LVO.

The ratio of the specific capacity at 8 A/g to that at 0.1 A/g is 24% for LVO, smaller than that of Vö-LVO (26%), indicating the better rate capability of Vö-LVO. Fig. 4b illustrates the cycling performance of the electrodes over 0.01–3 V at a current density of 1 A/g. Coulombic efficiencies of both Vö-LVO and LVO samples remained about 100% during the cycling process. The first coulombic efficiencies of Vö-LVO and LVO are 69% and 65%, respectively. The notable capacity decline primarily stems from irreversible side reactions occurring on the anode surface and interface. These encompass the formation of the SEI film and other irreversible consumption reactions involving lithium ions. After the capacity decline during the first several cycles, the capacity gradually increased. This may be attributed to the formation of a more stable solid electrolyte interface (SEI) film as the number of cycles increases, reducing the interfacial impedance and the side reactions with electrolyte, thereby enhancing the battery's capacity. The activation process of the active materials also contributes to the improved capacity [65]. After 500 cycles, Vö-LVO exhibits a capacity of 405 mAh/g with a retention of 90% (with respect to the first cycle), higher than that of LVO (236 mAh/g, 87% retention). The XRD patterns for both samples before and after the first cycle are shown in Fig. S11. After cycling, no extra peak appears in both samples, which implies no phase change happens after cycling, indicating the robust crystal structure. In addition, no significant peak shift occurs after the first cycle, which suggests the intercalation/de-intercalation of Li^+ almost does not change the lattice parameter, indicating the volume change during cycling is extremely small, which prevents the electrode from cracking and benefits the cycle stability. Notably, the lithium-storage capability of Vö-LVO is significantly better than that of LVO due to the introduction of oxygen vacancies. The cycling performance of Vö-LVO is more competitive in comparison with the reported Li_3VO_4-based anodes as listed in Table S5. Electrochemical impedance spectroscopy (EIS) was employed to explore enhanced conductivity and elucidate the underlying factors contributing to the improved electrochemical performance of the Vö-LVO electrode. As depicted in Fig. 4c, the EIS spectra comprise two distinct segments: a semicircle in the high-frequency region indicating the charge transfer resistance (R_{ct}) of the electrodes, and a straight line in the low-frequency region reflecting the diffusion of Li ions within the electrode bulk (Warburg resistance, W_o) [66]. An equivalent circuit, as shown in Fig. S12, was used to evaluate the values of R_{ct} of the two samples. Vö-LVO exhibits a noticeably reduced R_{ct} of 88.5 Ω compared to the LVO's 103.8 Ω, indicating a marked increase in the interfacial mass transfer kinetics attributed to the introduction of oxygen defects. Galvanostatic intermittent titration technique (GITT) is used to estimate the Li-ion diffusion coefficients (D_{Li^+}) of both samples in the charge and discharge process and the results are shown in Fig. 4d. The Vö-LVO electrode exhibited much higher lithium diffusion coefficients of $10^{-10.5--8.5}$ cm^2/s in comparison to the value of $10^{-11.2--10.2}$ cm^2/s in LVO during the discharge process. The promoted diffusion kinetics in Vö-LVO can be ascribed to the higher concentration of oxygen vacancies, weakening the interaction between Li^+ and electronegative lattice oxygen, and reducing the steric hindrance during ion diffusion [45]. The preceding outcomes of EIS and GITT distinctly reveal that the Vö-LVO sample, modified with oxygen defects, demonstrates a decreased charge-transfer resistance and an augmented lithium diffusion coefficient, thereby delivering significantly improved electrochemical performance. Li^+ ion diffusion energy barriers in Vö-LVO and LVO were calculated using the density functional theory (DFT) by simulating the Li^+ ion diffusion along the a-axis. Fig. 4e shows the migration paths and structures after Li^+ intercalation of Vö-LVO and perfect LVO without oxygen vacancy, respectively. Oxygen vacancies in Vö-LVO enlarge the ion diffusion channels to promote the diffusion of Li^+ along the a-axis. The maximum energy difference along the migration path is defined as the kinetic barrier, which is a good indicator of the Li^+ diffusion coefficient [67]. As shown in Fig. 4f, DFT calculations indicate that Vö-LVO exhibits a reduced diffusion energy barrier of 0.67 eV, in contrast to LVO (0.88 eV). This diminished migration energy barrier facilitates lithium-ion diffusion within the host lattice. The galvanostatic discharge and charge profiles of both samples are shown in Fig. S13. The difference between the profiles of the first cycle and the subsequent cycles can be ascribed to the formation of an SEI. Fig. S14 shows the voltage profiles at 3rd cycle of Vö-LVO and LVO electrodes at RT. Vö-LVO exhibits reduced polarization and an elevated specific capacity of 534 mAh/g, accompanied by a mid-value voltage of 0.74 V. These metrics surpass the specific capacity and voltage of LVO, which stand at 379 mAh/g and 0.61 V, respectively.

Fig. 5a illustrates the V 3d orbital splitting in symmetric and symmetry broken $[VO_4]$ tetrahedra, respectively. Oxygen vacancies in Vö-LVO break the local $[VO_4]$ symmetry, splitting the degenerate e orbitals into two non-degenerate orbitals, which act as the lowest unoccupied orbitals of Li_3VO_4 and determine its electrochemical potential. Due to this splitting, in Vö-LVO, the energy gap between e orbitals and the Fermi level of Li metal is increased compared with that of LVO, thereby leading to the increased electrochemical potential of Vö-LVO. The normalized voltage profiles of discharging and charging at RT for both samples are shown in Fig. 5b, c, respectively. The discharging mid-value voltage of Vö-LVO is higher than that of LVO by 0.13 V due to the lifted electrochemical potential of Vö-LVO as discussed above. Fig. 5c demonstrates that, although with a smaller polarization, Vö-LVO still has a higher mid-value voltage than LVO during charging, further confirming the altered ligand field induced by the broken local $[VO_4]$ symmetry. In addition, the broken symmetry also leads to the increase in the average V–O bond length, as shown in Fig. 2, decreasing the repulsion between the electrons of V and O, bringing V 3d orbitals to lower energy level and consequently improving the voltage, as illustrated in Fig. 3e. Fig. S15 shows the electrochemical performance of Vö-LVO and LVO at 0 °C. In Fig. S15a, both samples experience more significant polarization than that at RT due to the slower mass transfer, resulting in the diminished specific capacity. Under this condition, the discharging mid-value voltage of Vö-LVO is still higher than that of LVO by 0.14 V, as shown in Fig. S15b, further validating the lifted working voltage of Vö-LVO. Cyclic voltammetry (CV) curves of both samples were measured at a scan rate of 0.1 mV/s for three cycles in the voltage window of 0.01 to 3.00 V versus Li/Li^+ (Fig. S16). For the first three cycles, Vö-LVO and LVO exhibit similar electrochemical behaviors. The initial CV curve reveals a prominent reduction peak at 0.53 V attributed to Li^+ insertion during discharge. Additionally, two discernible oxidation peaks associated with the Li^+ deintercalation process appear around 1.10 and 1.33 V, aligning with the galvanostatic discharge-charge voltage profile. In the subsequent two cycles,

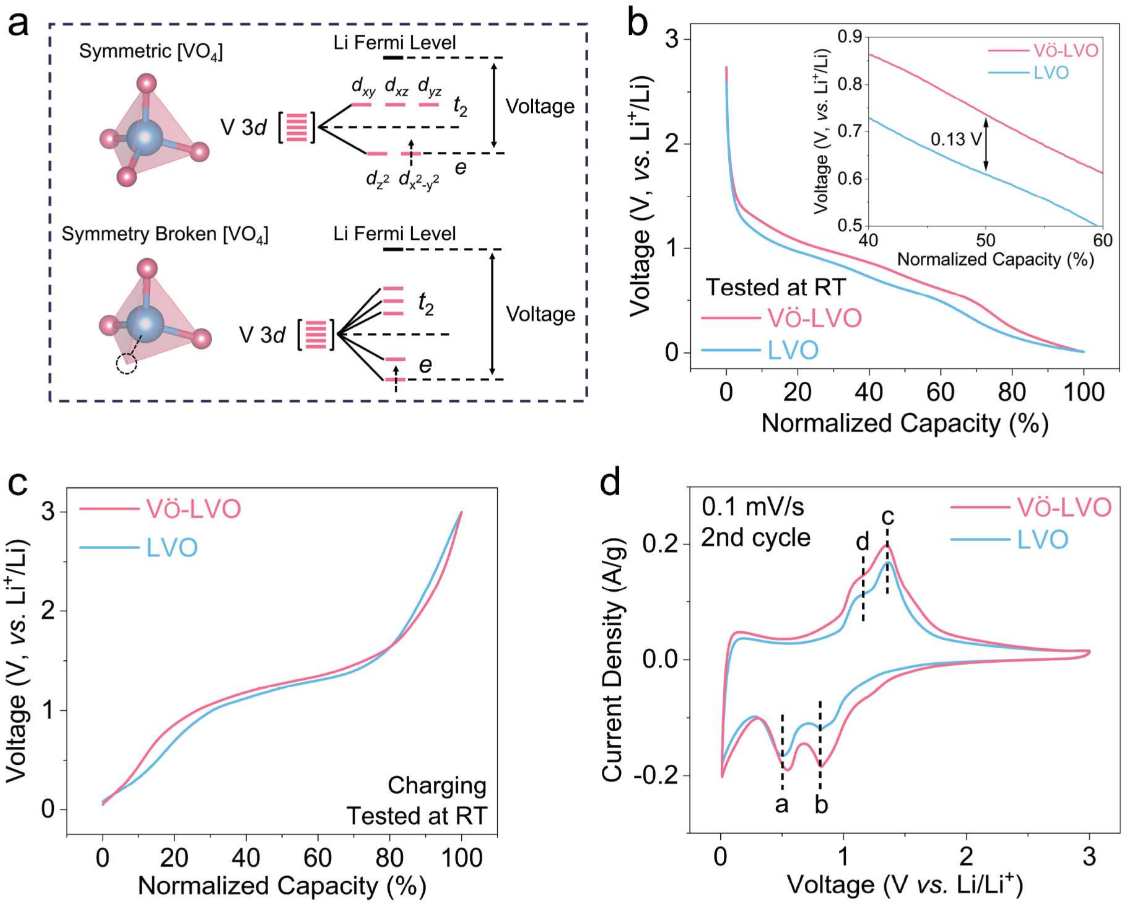

Figure 5 (a) Schematic diagram of the V 3d orbital splitting in symmetric and symmetry-broken [VO$_4$] tetrahedra. (b) Voltage versus normalized discharge capacity of Vö-LVO and LVO electrodes at RT. (c) Voltage versus normalized charge capacity of Vö-LVO and LVO electrodes at RT. (d) Comparison of the CV curves of the 2nd cycle at 0.1 mV/s for Vö-LVO and LVO.

the reduction peaks shift to 0.56 and 0.83 V, suggesting a multi-step Li$^+$ insertion process within the Vö-LVO following the initial cycle. Furthermore, the initially observed oxidation peak at 1.10 V gradually diminishes. The CV profile during the first cycle differs from those in the subsequent cycles, possibly attributed to the formation of an SEI and phase transformations [68]. Fig. 5d compares the CV curves of the 2nd cycle at 0.1 mV/s for both samples. The redox pairs and voltage differences are listed in Table S6. The reduced voltage differences observed in the redox pairs of Vö-LVO indicate smaller polarization and improved reaction kinetics in the electrochemical processes. The reduction peaks (peak a and peak b) of Vö-LVO shift to higher voltage by 0.04 and 0.01 V, respectively. While the oxidation peaks (peak c and peak d) of Vö-LVO nearly remain in the same positions as LVO's, although Vö-LVO has smaller polarization. This also demonstrates the increased working voltage of Vö-LVO. Various sweeping rates of CV curves of Vö-LVO are shown in Fig. S17a and no significant changes appear in the positions and shape of the current peaks with increasing sweeping rate. This indicates rapid Li$^+$ insertion/extraction kinetics in electrodes. Peak currents (i) and sweep rates (v) obey a power-law relationship that is described by $i = av^b$ (where a and b are variables). The b value can be determined by the slope of the log(v)-log(i) plots. A b value of 1 represents that the surface capacitance dominates the charge storage, whereas 0.5 indicates a diffusion-controlled process. The b values of peaks a–c in Vö-LVO are 0.79, 0.83, and 0.79 (Fig. S17c), whereas the values of peaks a–c from LVO are 0.67, 0.75, and 0.76 (Fig. S17d). These indicate that the majority of the currents at the peak potential of both samples are limited by ion diffusion and capacitor-like behavior. Fig. S18 shows the contributions of pseudocapacitance and ion diffusion control for Vö-LVO and LVO. As the scan rate increases from 0.3 to 1.2 mV/s, the capacitive contribution increases from 69% to 90%. In contrast, the capacitive contribution of pure LVO increases from 63% to 87%, indicating that both electrode materials exhibit pseudocapacitive-dominated fast charge storage characteristics at high scan rates.

CONCLUSIONS

The local coordination symmetry of [VO$_4$] tetrahedra in the bulk of Li$_3$VO$_4$ (Vö-LVO) is tailored by oxygen vacancies, which leads to the more significant splitting of ligand field and the decrease in energy level of the lowest unoccupied orbitals (e*), subsequently increasing the voltage output and narrowing the band gap. Additionally, DFT calculations corroborated an expanded ion diffusion channel and a reduced migration energy barrier in Vö-LVO. Thus, compared with pristine LVO, Vö-LVO shows reduced charge transfer resistance and improved Li$^+$ diffusion coefficient. Vö-LVO delivers a specific capacity of 532 mAh/g at 0.1 A/g, showcasing a remarkable 35% capacity enhancement when compared to 394 mAh/g of LVO. The uncovered fundamentals provide insights and guides into optimizing the electrode materials via modulating the local structure and ligand field.

Received 22 June 2025; accepted 18 September 2025;

1 Wang CY, Liu T, Yang XG, *et al.* Fast charging of energy-dense lithium-ion batteries. Nature, 2022, 611: 485–490

2 Wolf A, Nagler F, Daubinger P, *et al.* Circular battery design: investing in sustainability and profitability. Energy Environ Sci, 2024, 17: 8529–8544

3 Frith JT, Lacey MJ, Ulissi U. A non-academic perspective on the future of lithium-based batteries. Nat Commun, 2023, 14: 420

4 Zou P, Sui Y, Zhan H, *et al.* Polymorph evolution mechanisms and regulation strategies of lithium metal anode under multiphysical fields. Chem Rev, 2021, 121: 5986–6056

5 Bi J, Du Z, Sun J, *et al.* On the road to the frontiers of lithium-ion batteries: a review and outlook of graphene anodes. Adv Mater, 2023, 35: 2210734

6 Obrovac MN, Chevrier VL. Alloy negative electrodes for Li-ion batteries. Chem Rev, 2014, 114: 11444–11502

7 Li Y, Lu Y, Adelhelm P, *et al.* Intercalation chemistry of graphite: alkali metal ions and beyond. Chem Soc Rev, 2019, 48: 4655–4687

8 Noel M, Santhanam R. Electrochemistry of graphite intercalation compounds. J Power Sources, 1998, 72: 53–65

9 Kim H, Choi W, Yoon J, *et al.* Exploring anomalous charge storage in anode materials for next-generation Li rechargeable batteries. Chem Rev, 2020, 120: 6934–6976

10 Finegan DP, Quinn A, Wragg DS, *et al.* Spatial dynamics of lithiation and lithium plating during high-rate operation of graphite electrodes. Energy Environ Sci, 2020, 13: 2570–2584

11 Zhang H, Yang Y, Xu H, *et al.* $Li_4Ti_5O_{12}$ spinel anode: fundamentals and advances in rechargeable batteries. InfoMat, 2021, 4: e12228

12 Thackeray MM, Amine K. $Li_4Ti_5O_{12}$ spinel anodes. Nat Energy, 2021, 6: 683

13 Yuan T, Tan Z, Ma C, *et al.* Challenges of spinel $Li_4Ti_5O_{12}$ for lithium-ion battery industrial applications. Adv Energy Mater, 2017, 7: 1601625

14 Wang K, Zhang C, Fu H, *et al.* Enhanced electrochemical properties of Li_3VO_4 with controlled oxygen vacancies as Li-ion battery anode. Chem Eur J, 2017, 23: 5368–5374

15 Li H, Liu X, Zhai T, *et al.* Li_3VO_4: a promising insertion anode material for lithium-ion batteries. Adv Energy Mater, 2012, 3: 428–432

16 Liao C, Wen Y, Xia Z, *et al.* Si-doping mediated phase control from β- to γ-form Li_3VO_4 toward smoothing Li insertion/extraction. Adv Energy Mater, 2018, 8: 1701621

17 Shen L, Chen S, Maier J, *et al.* Carbon-coated Li_3VO_4 spheres as constituents of an advanced anode material for high-rate long-life lithium-ion batteries. Adv Mater, 2017, 29: 1701571

18 Liu X, Li G, Qian P, *et al.* Carbon coated Li_3VO_4 microsphere: ultrafast solvothermal synthesis and excellent performance as lithium-ion battery anode. J Power Sources, 2021, 493: 229680

19 Hsiao YS, Huang JH, Weng LY, *et al.* Advancing Li_3VO_4 as a high-performance anode material for use in lithium-ion batteries and lithium-ion capacitors. Chem Eng J, 2024, 489: 150973

20 Du CQ, Wu JW, Liu J, *et al.* Synthesis of lithium vanadium tetroxide anode material via a fast sol-gel method based on spontaneous chemical reactions. Electrochim Acta, 2015, 152: 473–479

21 Ni S, Lv X, Ma J, *et al.* Electrochemical characteristics of lithium vanadate, Li_3VO_4 as a new sort of anode material for Li-ion batteries. J Power Sources, 2014, 248: 122–129

22 Liang Z, Zhao Y, Ouyang L, *et al.* Synthesis of carbon-coated Li_3VO_4 and its high electrochemical performance as anode material for lithium-ion batteries. J Power Sources, 2014, 252: 244–247

23 Zhang C, Song H, Liu C, *et al.* Fast and reversible Li ion insertion in carbon-encapsulated Li_3VO_4 as anode for lithium-ion battery. Adv Funct Mater, 2015, 25: 3497–3504

24 Zhang C, Liu C, Nan X, *et al.* Hollow–cuboid Li_3VO_4/C as high-performance anodes for lithium-ion batteries. ACS Appl Mater Interfaces, 2015, 8: 680–688

25 Hu S, Song Y, Yuan S, *et al.* A hierarchical structure of carbon-coated Li_3VO_4 nanoparticles embedded in expanded graphite for high performance lithium ion battery. J Power Sources, 2016, 303: 333–339

26 Shi Y, Wang JZ, Chou SL, *et al.* Hollow structured Li_3VO_4 wrapped with graphene nanosheets *in situ* prepared by a one-pot template-free method as an anode for lithium-ion batteries. Nano Lett, 2013, 13: 4715–4720

27 Liu J, Lu PJ, Liang S, *et al.* Ultrathin Li_3VO_4 nanoribbon/graphene sandwich-like nanostructures with ultrahigh lithium ion storage properties. Nano Energy, 2015, 12: 709–724

28 Jian Z, Zheng M, Liang Y, *et al.* Li_3VO_4 anchored graphene nanosheets for long-life and high-rate lithium-ion batteries. Chem Commun, 2015, 51: 229–231

29 Li Q, Wei Q, Sheng J, *et al.* Mesoporous Li_3VO_4/C submicron-ellipsoids supported on reduced graphene oxide as practical anode for high-power lithium-ion batteries. Adv Sci, 2015, 2: 1500284

30 Huang Y, Yang H, Zhang Y, *et al.* A safe and fast-charging lithium-ion battery anode using MXene supported Li_3VO_4. J Mater Chem A, 2019, 7: 11250–11256

31 Liang G, Yang L, Han Q, *et al.* Conductive $Li_{3.08}Cr_{0.02}Si_{0.09}V_{0.9}O_4$ anode material: novel "zero-strain" characteristic and superior electrochemical Li^+ storage. Adv Energy Mater, 2020, 10: 1904267

32 Dong Y, Duan H, Park K, *et al.* Mo^{6+} doping in Li_3VO_4 anode for Li-ion batteries: significantly improve the reversible capacity and rate performance. ACS Appl Mater Interfaces, 2017, 9: 27688–27696

33 Dong Y, Zhao Y, Duan H, *et al.* $Li_{2.97}Mg_{0.03}VO_4$: high rate capability and cyclability performances anode material for rechargeable Li-ion batteries. J Power Sources, 2016, 319: 104–110

34 Liao C, Zhang Q, Zhai T, *et al.* Development and perspective of the insertion anode Li_3VO_4 for lithium-ion batteries. Energy Storage Mater, 2017, 7: 17–31

35 Zhu L, Li Z, Ding G, *et al.* Review on the recent development of Li_3VO_4 as anode materials for lithium-ion batteries. J Mater Sci Tech, 2021, 89: 68–87

36 Zhao D, Cao M. Constructing highly graphitized carbon-wrapped Li_3VO_4 nanoparticles with hierarchically porous structure as a long life and high capacity anode for lithium-ion batteries. ACS Appl Mater Interfaces, 2015, 7: 25084–25093

37 Li Q, Wei Q, Wang Q, *et al.* Self-template synthesis of hollow shell-controlled Li_3VO_4 as a high-performance anode for lithium-ion batteries. J Mater Chem A, 2015, 3: 18839–18842

38 Li Q, Sheng J, Wei Q, *et al.* A unique hollow Li_3VO_4/carbon nanotube composite anode for high rate long-life lithium-ion batteries. Nanoscale, 2014, 6: 11072–11077

39 Ni S, Zhang J, Lv X, *et al.* Superior electrochemical performance of Li_3VO_4/NiO/Ni electrode via a coordinated electrochemical reconstruction. J Power Sources, 2015, 291: 95–101

40 Qin R, Shao G, Hou J, *et al.* One-pot synthesis of Li_3VO_4@C nanofibers by electrospinning with enhanced electrochemical performance for lithium-ion batteries. Sci Bull, 2017, 62: 1081–1088

41 Zhao L, Duan H, Zhao Y, *et al.* High capacity and stability of Nb-doped Li_3VO_4 as an anode material for lithium ion batteries. J Power Sources, 2018, 378: 618–627

42 Zhang C, Wang K, Liu C, *et al.* Effects of high surface energy on lithium-ion intercalation properties of Ni-doped Li_3VO_4. NPG Asia Mater, 2016, 8: e287

43 Zhang Y, Tao L, Xie C, *et al.* Defect engineering on electrode materials for rechargeable batteries. Adv Mater, 2020, 32: 1905923

44 Khossossi N, Singh D, Ainane A, *et al.* Recent progress of defect chemistry on 2D materials for advanced battery anodes. Chem An Asian J, 2020, 15: 3390–3404

45 Guo C, Yi S, Si R, *et al.* Advances on defect engineering of vanadium-based compounds for high-energy aqueous zinc–ion batteries. Adv Energy Mater, 2022, 12: 2202039

46 Wang D, Jiao Y, Shi W, *et al.* Fundamentals and advances of ligand field theory in understanding structure-electrochemical property relationship of intercalation-type electrode materials for rechargeable batteries.

Prog Mater Sci, 2023, 133: 101055
47 Wang Y, Cai J, Wu M, *et al.* Rational construction of oxygen vacancies onto tungsten trioxide to improve visible light photocatalytic water oxidation reaction. Appl Catal B-Environ, 2018, 239: 398–407
48 Lu X, Zeng Y, Yu M, *et al.* Oxygen-deficient hematite nanorods as high-performance and novel negative electrodes for flexible asymmetric supercapacitors. Adv Mater, 2014, 26: 3148–3155
49 Yuan Y, Ma J, Su Y, *et al.* Tailoring local chemical coordination in vanadium pentoxide to enable high efficiency zinc ion storage. J Electrochem Soc, 2023, 170: 110515
50 Julien C, Massot M, Pérez-Vicente C. Structural and vibrational studies of $LiNi_{1-y}Co_yVO_4$ ($0\leqslant y\leqslant 1$) cathodes materials for Li-ion batteries. Mater Sci Eng-B, 2000, 75: 6–12
51 Kim DJ, Jun BE, Kim CS, *et al.* Dielectric properties of Li_3VO_4 single crystals grown by the Czochralski method. J Appl Phys, 2003, 93: 1697–1700
52 Tao Y, Yi D, Li J. Electrochemical formation of crystalline Li_3VO_4/Li_4SiO_4 solid solutions film. Solid State Ion, 2008, 179: 2396–2398
53 Yang G, Zhang B, Feng J, *et al.* Morphology controlled lithium storage in Li_3VO_4 anodes. J Mater Chem A, 2018, 6: 456–463
54 Zhao X, Li L, Zheng L, *et al.* 3d-orbital regulation of transition metal intercalated vanadate as optimized cathodes for calcium-ion batteries. Adv Funct Mater, 2023, 34: 2309753
55 Gaur A, Shrivastava BD. Speciation using X-ray absorption fine structure (XAFS). Ref J Chem, 2015, 5: 361–398
56 Avansi W, Maia LJQ, Ribeiro C, *et al.* Local structure study of vanadium pentoxide 1D-nanostructures. J Nanopart Res, 2011, 13: 4937–4946
57 Tian M, Liu C, Zheng J, *et al.* Structural engineering of hydrated vanadium oxide cathode by K^+ incorporation for high-capacity and long-cycling aqueous zinc ion batteries. Energy Storage Mater, 2020, 29: 9–16
58 Adamski A, Spałek T, Sojka Z. Application of EPR spectroscopy for elucidation of vanadium speciation in VO_x/ZrO_2 catalysts subject to redox treatment. Res Chem Intermed, 2003, 29: 793–804
59 Kittel C. Introduction to Solid State Physics. New York: Wiley, 2004
60 Liu H, Niu H, Huang WH, *et al.* Unveiling the local structure and the ligand field of organic cation preintercalated vanadate cathode for aqueous zinc-ion batteries. ACS Energy Lett, 2024, 9: 5492–5501
61 Niu H, Liu H, Yang L, *et al.* Impacts of distorted local chemical coordination on electrochemical performance in hydrated vanadium pentoxide. Nat Commun, 2024, 15: 9421
62 Liu H, Hou X, Fang T, *et al.* Boosting zinc-ion storage in hydrated vanadium oxides via migration regulation. Energy Storage Mater, 2023, 55: 279–288
63 Brown T, LeMay H, Bursten B, *et al.* Chemistry: the Central Science. Boston: Pearson, 2017
64 Abbate M, Pen H, Czyżyk MT, *et al.* Soft X-ray absorption spectroscopy of vanadium oxides. J Electron Spectr Relat Phenomena, 1993, 62: 185–195
65 Yoshio M, Brodd R, Kozawa A. Lithium-ion Batteries: Science and Technologies. New York: Springer, 2009
66 Lazanas AC, Prodromidis MI. Electrochemical impedance spectroscopy—a tutorial. ACS Meas Sci Au, 2023, 3: 162–193
67 Huang G, Zhang Z, Kang K, *et al.* Al_4C_3 growth mechanism based on diffusion of carbon atoms: first-principles study. Mater Today Commun, 2023, 37: 107591
68 Goodenough JB, Kim Y. Challenges for rechargeable Li batteries. Chem Mater, 2009, 22: 587–603

Acknowledgement This work was financially supported by the Natural Science Foundation of Fujian Province (2022J011269), the National Natural Science Foundation of China (52102277, 52472238, 52302193), the Fujian Provincial Key Laboratory of Functional Materials and Applications (fma2022005), and the Fundamental Research Funds for the Central Universities, conducted by Tongji University. The synchrotron radiation PDF experiments were performed at BL02B1 of SPring-8 with the approval of Japan Synchrotron Radiation Research Institute (JASRI, Proposal No. 2024A1878).

Author contributions Ma J and Liu H contributed primarily to this work. Kang T and Niu H offered help for experimental sections. Li C and Yang L assisted the calculations section. Liu C and Cao G are corresponding writers. This manuscript was written through the contributions of all authors. All authors have given approval to the final version of the manuscript.

Conflict of interest The authors declare that they have no conflict of interest.

Supplementary information Supplementary materials are available in the online version of the paper.

Jidong Ma is currently working as an associate professor at Xiamen University of Technology. Her recent research focuses on the development of advanced nanomaterials, the development and application of advanced powder metallurgy materials, metal injection molding (MIM) of soft magnetic materials, and advanced energy materials.

Heng Liu is currently a Master's student at Tongji University. His research interests focus on the vanadium-based cathode/anode materials for ZIBs and LIBs.

Chaofeng Liu is currently working as an assistant professor at School of Materials Science and Engineering, Tongji University. His research interests focus on the fundamental studies of electrode materials for electrochemical energy storage, especially deciphering the relationship between the electrochemical potential and crystal field.

Guozhong Cao is the Boeing-Steiner professor of Materials Science and Engineering and Chemical Engineering and adjunct professor of Mechanical Engineering at the University of Washington. His current research mainly focuses on chemical processing and characterization of nanostructured materials and coatings for energy related applications as well as biosensors and biomedical applications.

配位场调控改善Li_3VO_4材料的锂离子电池电化学性能

麻季冬[1,2†], 刘恒[3†], 康特[3], 李昌源[3], 牛欢欢[3], 杨龙[3], 刘超峰[2,3*], 曹国忠[2*]

摘要 电极材料的电化学势和离子扩散特性制约着锂离子电池的能量密度与功率密度, 嵌入型Li_3VO_4 (LVO)材料面临同样的挑战. 本研究通过引入更高浓度的氧空位(Vo), 诱发LVO中$[VO_4]$的配位不对称性, 增长V–O平均键长及增大配体场分裂程度. 进而, 实现最低未占据轨道(e^*)能级的降低, 提升材料的电化学势. 此外, 研究发现氧空位修饰的LVO (Vo-LVO)因为局部对称性降低, 导致带隙减小, 以及离子传输通道拓宽, 从而改善电化学储能反应过程中的动力学特性. 局部对称性破缺的Vo-LVO在0.1 A/g的电流密度下展现出显著提升的比容量532 mAh/g, 高于未改性LVO的394 mAh/g. 在1 A/g的电流密度下经过500次循环后, Vo-LVO比容量保持为398 mAh/g, 而LVO仅为236 mAh/g, 体现出优异的循环稳定性. 这一基础研究成果为通过配体场工程开发高性能电极材料、助力下一代可充电电池的发展提供了重要思路.